https://doi.org/10.33263/BioMed21.030048

ISSN: 2668-6007 https://biomedicalengineering.international

Biomedical Engineering International

Volume 2, Issue 1, Pages 0030-0048
2020

Article

Received: 27.03.2020
Accepted: 04.04.2020
Published: 08.04.2020

Phosphonopropionic acid coating as platform for the efficient grafting of (bio)molecules to hydroxyapatite nanoparticles

María Laura Dittler [1], Hernán B. Rodríguez [1,*], Mariano Cipollone [2], Claudia A. Grillo [1] and Mónica C. Gonzalez [1,*]

[1] Instituto de Investigaciones Fisicoquímicas Teóricas y Aplicadas (INIFTA), CCT-La Plata-CONICET, Universidad Nacional de La Plata, La Plata, Argentina; mlauradittler@quimica.unlp.edu.ar; cgrillo@inifta.unlp.edu.ar
[2] YPF Tecnología S.A. Baradero S/N (1925) Ensenada - Bs As., Argentina; mariano.cipollone@ypftecnologia.com

* Correspondence: hernanrodriguez@inifta.unlp.edu.ar Scopus ID 12766535500
gonzalez@inifta.unlp.edu.ar Scopus ID 26661104400

Abstract: A new synthesis strategy intended to increase apatite available surface groups for the covalent functionalization with (bio)molecules was developed. To that purpose, hydroxyapatite nanoparticles (Ap) were synthesized and terminated with 3-phosphonopropionic acid (PPA) yielding Ap with surface bound propionic acid through P-C bonds (ApCOO⁻). A thorough characterization of ApCOO⁻ by IR spectroscopy, transmission electron microscopy, X-ray diffraction, X-ray photoelectron spectroscopy, thermal gravimetric analysis, and specific surface area determination (BET model), strongly support an efficient surface grafting of the organophosphonates and a hydroxyapatite core of similar morphology and phase composition to that of synthetic Ap. ApCOO⁻ was able to adsorb bovine serum albumin (BSA) up to 0.20 mg m^{-2} and showed no cytotoxic effects towards Balb/C 3T3 cells. ApCOO⁻ abundant carboxyl surface groups facilitated the particles grafting through stable amide bonds with basic fuchsin (Fu) and tyrosine (Ty) yielding well covered surfaces. Fu-bound hydroxyapatite powders showed ten times stronger fluorescence than free Fu in ethanol, thus expanding the potential uses of Ap as fluorescent sensors in the red region of the visible spectrum. On the other hand, Ty-bound hydroxyapatite powders showed negative surface charges and high stability of the coating in aqueous suspensions. In contrast, Ty-physically adsorbed hydroxyapatite powders rendered positively charged surfaces and an unstable coating.

Keywords: hydroxyapatite nanoparticles; propionic acid-terminated; tyrosine-grafted; fuchsin-grafted; fluorescence.

1. Introduction

Because of their high biocompatibility and similar chemical structure and biomimetic features to that of the mineral phase of hard biological tissues, hydroxyapatite nanoparticles (Ap) is used in

Cite This Article: Dittler, M.L.; Rodríguez, H.B.; Cipollone, M.; Grillo, C.A.; Gonzalez, M.C. Phosphonopropionic acid coating as platform for the efficient grafting of (bio)molecules to hydroxyapatite nanoparticles. Biomed Eng Int **2020**, 2, 0030-0048. https://doi.org/10.33263/BioMed21.030048

a number of different tissue engineering applications [1,2] and as a vehicle for drug delivery [3]. Surface functionalization is a widely used strategy to enhance the positive biological response of synthetic apatite [3-6]. To date, the main effort towards the covalent functionalization of synthetic apatite is directed to overcome the available surface groups of crystalline apatite. Among the different reported strategies are the synthesis of apatite in the presence of amino acids [7], polycondensation of substituted alkoxysilanes on the apatite surface [8], grafting of organophosphonates ($RP(O)(OH)_2$ with R = n-alkyl chain) [9,10], and apatite synthesis in the presence of carboxylate-bearing organic molecules [11].

In particular, surface modification of pre-formed apatite materials with low concentrations of organophosphonic acids has been reported to form disordered monolayers of covalently attached organophosphonic groups via P−O−P bonds, while solutions of higher concentrations led to a bulk modification of apatite with a high loading of organics [9]. Moreover, the "one pot" mixture of inorganic phosphates and alkylphosphonates during apatite synthesis is reported to generate mesoporous materials with high specific surface area and significant loss of crystallinity [10]. These studies are in line with early investigations reporting an inhibiting effect of low concentrations of phosphonates towards hydroxyapatite crystallites growth [12].

Among the molecules used to coat hydroxyapatite materials, those bearing COO^- functional groups deserve special attention as carboxylates have been shown to promote important biological processes in bone tissue engineering [13] and the induction of calcium phosphate mineralization [14,15]. Also, carboxyl functional groups may be easily activated to form peptide bonds [16] with amino acids and proteins to yield apatite materials with enhanced biological activity [17]. Formation of peptide bonds between the COOH bearing apatite and amino acids assures a constant and stable composite formulation upon mild changes in pH, temperature, ionic strength, and other (bio)molecules present in suspension, which is not expected in systems where the amino acid is physically adsorbed [18]. Also, the nature of the remaining surface charge might be different, since in adsorbed composites the α-carboxylate of the amino acid is preferentially bound to the apatite structure rendering more positively charged surfaces [19], while formation of peptide bonds between COOH bearing apatite and amino acids leaves free α-carboxylates groups which support a more negative surface charge.

Based on the previous discussion and with the aim of obtaining Ap with a plethora of surface groups but conserving Ap morphological properties, we developed a new synthetic strategy using 3-phosphonopropionic acid (PPA) to obtain versatile propionate-coated nanohydroxyapatite ($ApCOO^-$), capable of being used as building blocks for the preparation of bioinorganic nanocomposites. $ApCOO^-$ cell viability was tested and its interaction with bovine serum albumin (BSA) proteins was evaluated, comparing results with those of Ap, in order to assess propionate-coating effects on protein adsorption and cytotoxicity. To probe the versatility of $ApCOO^-$ particles as precursors in the synthesis of more complex surface-functionalized apatite-based materials, further derivatizations with basic fuchsin (Fu), a fluorescent dye commonly used for staining purposes in biomedical research, and with tyrosine (Ty), a fluorescent amino acid, were performed. Fluorescent Ap are of interest [20–22] in fields such as cell labeling, animal imaging and therapy, and drug delivery and release.

On the other hand, Ty is a versatile amino acid that plays several important roles in biological systems [23]. The phenolic side chain of Ty and its unique chemical reactivity enable its involvement in many molecular interactions and biosynthetic transformations as interactions with metal ions in the active centers of enzymes and hydrogen bonding of Ty to surround residues and further concerted proton and electron transfer. Moreover, exploitation of the oxidation chemistry of the phenolic side chain of Ty to various forms, such as dityrosine cross-linking endows the systems with enhanced structural properties, such as resilience and a high fatigue lifetime. Therefore, coating of Ap with Ty may open potential properties to hydroxyapatite-based materials.

2. Materials and Methods

The list of Materials, details of the standard Equipment and Physicochemical assays used for particle characterization, and BSA adsorption and release on Ap and $ApCOO^-$ (10%) are provided in the Supplementary Material under the titles "Materials", "Equipment", and "Loading of BSA", respectively. Biological standard procedures, including cell cultures used and cell viability assays (AO staining and MTT assay) are also depicted as Supplementary Material.

2.1. Synthesis of Ap

15 mL of a solution containing 0.981 g H_3PO_4 was added drop-wise into 10 mL $Ca(OH)_2$ suspension (125 g L^{-1}) over a period of 30 minutes under constant stirring and heating at 80°C. The mixture was then allowed to stand stirring at room temperature for one hour. The obtained Ap was separated from the mother liquor by filtration with hydrophilic 0.22 μm pore membranes, washed several times with deionized water, and dried at 80°C for 24 h.

2.2. Synthesis of $ApCOO^-$

The synthesis of $ApCOO^-$ involved a one-pot procedure where the molar Ca:inorganic P = 1.67 ratio was maintained. Briefly, 15 mL of a solution containing 0.981 g H_3PO_4 was added drop-wise into 10 mL of 125 g L^{-1} $Ca(OH)_2$ suspension to initiate Ap formation over a period of 30 minutes under constant stirring and heating at 80°C. Subsequently, 0.165 (or 0.083) g of PPA were added to the mixture, the suspension was stirred at room temperature for 3 h, and the particles separated from the mother liquor by filtration with a 0.22 μm hydrophilic membrane and washed with deionized water until no absorbance between 250-300 nm was observed in the washing liquors. To differentiate the particles obtained from each synthesis batch, the mole percent fraction of organic P to total P used in the synthesis procedure is indicated following the particle name, i.e. $ApCOO^-$ (10%) and $ApCOO^-$ (5%). Particles stored in aqueous suspensions at 40°C for 48 h showed constant pH and absorbance between 250-300 nm in the liquid phase (see Supplementary Material under the title "$ApCOO^-$ Stability"), strongly supporting a high stability towards PPA elimination from the apatite surface.

2.3. Ty immobilization on $ApCOO^-$ (10%)

Ty covalent grafting to $ApCOO^-$ (10%) nanoparticles was performed through the coupling reaction between the particles carboxylates and the amine groups of the amino acid catalized by N,N´-dicyclohexylcarbodiimide (DCC) [24]. Secondary reactions were avoided protecting Ty carboxyl group by esterification with benzyl alcohol. To that purpose, 1.5 g of L-Ty was mixed with 4 mL HCl and 40 mL benzyl alcohol and the resulting solution maintained at 81°C for *ca.* 1 hour before product extraction with ethyl ether and 10% HCl aqueous solutions. The pH of the remaining aqueous phase was adjusted to 9.1 by NH_4OH addition. The precipitated Ty benzyl ester solid was isolated by filtration with 0.22 μm hydrophilic membranes and washed with ethanol.

To activate the particles carboxylic groups, 4 mg DCC and 4 mg N-hydroxysuccinimide (NHS) were added to 10 mL of an ethanol suspension of $ApCOO^-$ (10%) (1 g L^{-1}) and the mixture was left stirring at room temperature in the dark for 18 h. Subsequently, 5 mg of Ty benzyl ester was added, and the coupling reaction left to proceed for 72 h under constant stirring. The particles were separated from the reactive mixture by filtration with a 0.22 μm hydrophilic membrane and washed with ethanol until no absorbance at 350 nm was observed in the washing liquors. The benzyl ester group was then hydrolyzed in a phosphate buffer of pH 6.8 and 0.125 M ionic strength, at 60°C for 24 h [25]. The obtained surface-modified particles, denoted as ApCOOTy, were kiln-dried at 60°C during 24 h.

On the other hand, Ap covered with Ty by physical adsorption were obtained for comparison purposes. To that purpose, 5 mg of Ty were mixed with 10 mL of an aqueous suspension of Ap (1 g L^{-1}) and the mixture was left stirring at room temperature in the dark for 48 h. The coated particles were separated from the reaction mixture by filtration with a 0.22 μm hydrophilic membrane and washed with water. Ty is observed to slowly desorb with time when Ty-adsorbed apatite powders were resuspended in pure water, as observed from variations in the Z-potential of the particles and an increased absorbance of the suspension filtrate.

2.4. Fu immobilization on ApCOO⁻ (10%)

Freshly prepared ApCOO⁻ (10%) particles (*vide supra*) were surface derivatized with Fu involving amide bonding, following a similar procedure as described for Ty derivatization but adding 2 mg Fu. To eliminate adsorbed Fu traces, the conjugated nanoparticles, ApCOOFu, were resuspended in ethanol, filtered with 0.22 μm filters, and washed. The latter cycle was repeated until washing liquids did not show traces of Fu by UV-vis absorption spectroscopy. ApCOOFu particles remained as a red solid filtrate on 0.22 μm membranes, as shown in the Supplementary Material under the title "ApCOOFu coloured filtrates". Blank experiments performed with Fu and ApCOO⁻ in the absence of DCC and NHS, showed that Fu does not remain physically adsorbed on ApCOO⁻ after thorough washing. Altogether these observations support an efficient Fu covalent grafting to ApCOO⁻.

Figure 1 illustrates the particular surface chemistry of the obtained hydroxyapatite-based particles, as a guide to help understand the following results.

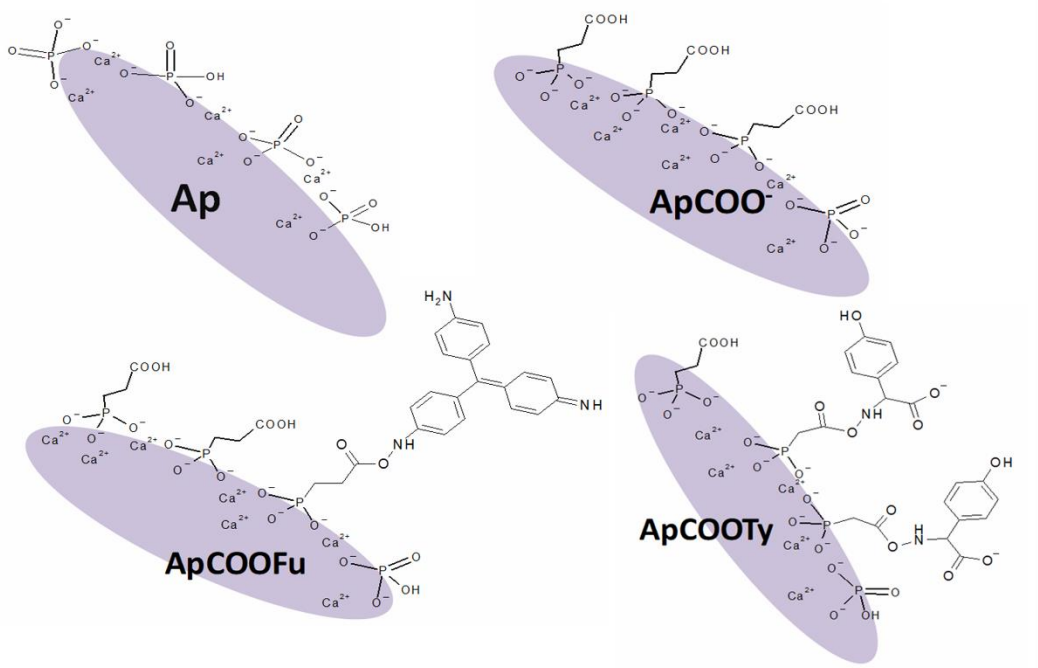

Figure 1. Illustrative surface representation of Ap, ApCOO⁻, ApCOOFu, and ApCOOTy.

3. Results and Discussion

3.1. Ap and ApCOO⁻ characterization

High Resolution Transmission Electron Microscopy (HRTEM) images of Ap, ApCOO⁻ (5%), and ApCOO⁻ (10%) depicted in Figure 2 revealed the formation of highly crystalline rod-shaped Ap with lattice spacings of *ca.* 0.34 nm, align along the particle long axis, in line with those reported for hydroxyapatite (002) planes [26]. Rods are of 10-20 nm width and between 50-100 nm long. Because of agglomeration, it was not possible to determine the size distribution of the particles.

Corresponding XRD diffractograms of Ap, ApCOO⁻ (5%) and ApCOO⁻ (10%) are shown in Figure 3. All spectra showed patterns and peak widths characteristic to hydroxyapatite powders [27]. Impurity phases such as α- and β-tricalcium phosphate (TCP), if present, are at very low levels as no significant contribution of TCP most intense peaks at 2θ = 30.5-31.6 are observed [28]. These observations clearly suggest that mainly hydroxyapatite crystalline domains are formed upon the late addition of 5 and 10% PPA during synthesis.

Figure 4A shows the ATR-IR spectra of Ap, ApCOO⁻ (5%), and ApCOO⁻ (10%). The spectrum of Ap shows the fundamental vibration modes of PO_4 groups of the apatitic nanocrystalline structure at about 960, and 1010-1100 cm^{-1} [29]. Small bands

at 875 and 1460-1420 cm^{-1} attributed to residual carbonate from the synthesis process are also observed [30]. The ATR-IR spectrum of both $ApCOO^-$ (5%) and $ApCOO^-$ (10%) also depict Ap characteristic bands. However, while $ApCOO^-$ (5%) mainly shows these bands, the spectrum of $ApCOO^-$ (10%) also depicts the presence of new peaks at 2925-2850, 1440-1410, 1320, and 800 cm^{-1} due to methylene symmetric and asymmetric stretching, CO stretching in carboxylic acid salts [31], P-CH_2R, and C-O vibrations [32], respectively, thus confirming the presence of P-bonded propionate groups on $ApCOO^-$ (10%) surface.

Considering that $ApCOO^-$ (10%) shows the presence of abundant surface P-bonded propionate groups while maintaining the crystalline structure of Ap, all further studies will be described for these particles.

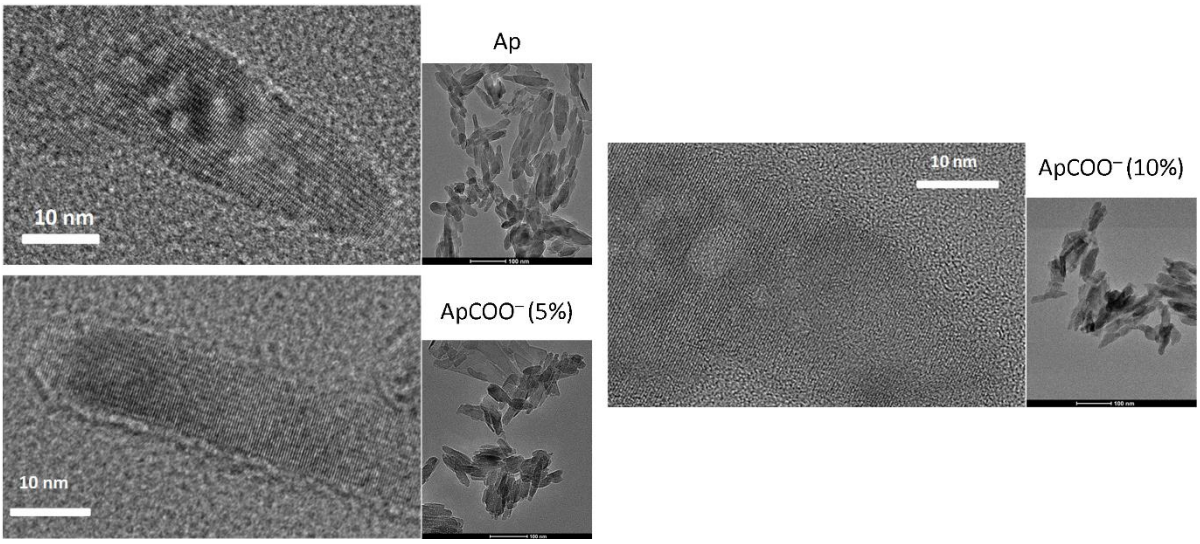

Figure 2. HRTEM micrographs of Ap, $ApCOO^-$ (5%), and $ApCOO^-$ (10%).

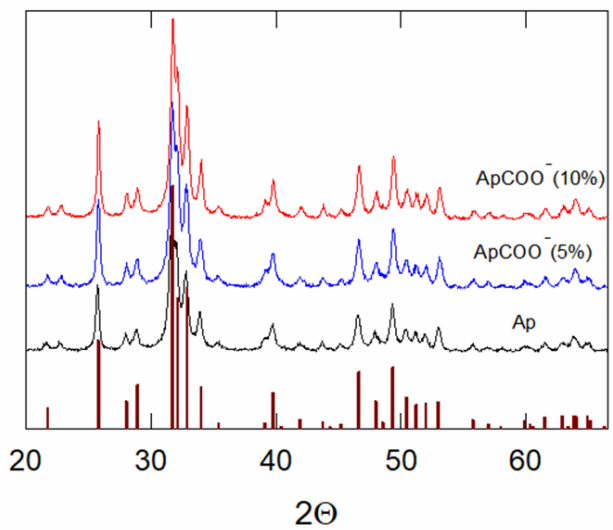

Figure 3. X-ray diffractograms of Ap, ApCOO- (5%), and ApCOO- (10%), from bottom to top, respectively. Bars stand for synthetic hydroxyapatite principal reference pattern [27].

TGA analysis of Ap (Figure 4B) obtained in an O_2 environment in the temperature range from 100 to 650°C yield information on adsorbed substrates, as decomposition of the Ap structure is expected to occur at temperatures over 800°C when the dehydration processes start taking place [29]. The about 6.3% total mass loss of Ap in the temperature range from 100 to 520°C may be attributed to loss of adsorbed and lattice water and the 1.7% loss between 450-650°C to the elimination of surface

carbonate-like groups, in good agreement with literature reports for nano-sized Ap powders [33].

ApCOO⁻ (10%) shows a different loss pattern than Ap (Figure 4B) at temperatures between 120 and 440°C, which may be attributed to the presence of organic matter. The mass loss of ~7% observed in this temperature range may be assigned to the oxidation of the propyl carboxylate groups to CO_2. However, the contribution to the mass loss due to lattice water cannot be neglected. Moreover, a further loss of 1.4% is observed in the temperature range between 450-650°C, attributed to the elimination of surface carbonate-like groups, in agreement with that of Ap. Therefore, considering that lattice water mass might be on the same order as that of Ap, *ca.* 0.055 moles of propionic acid groups per 100 g of ApCOO⁻ (10%) is estimated. Considering the measured specific surface area of 67.5 $m^2\ g^{-1}$ for ApCOO⁻ (10%), an area of ~20 $Å^2$ per propionic acid group is estimated, which is in the order of the cross sectional area of aliphatic carboxylic acids in a water/air film interface [34], thus indicating a well-covered surface with PPA.

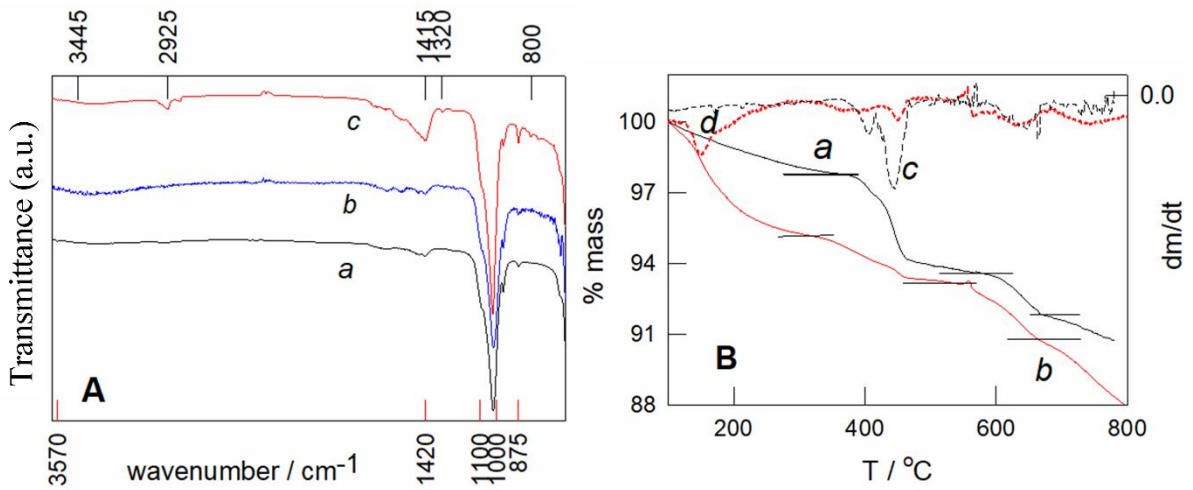

Figure 4. (A) ATR-IR spectra of Ap (black lines, curve a), ApCOO⁻ (5%) (blue lines, curve b), and ApCOO⁻ (10%) (red lines, curve c). (B) TGA performed in oxygen atmosphere of Ap (black line, curve a), ApCOO⁻ (10%) (red lines, curve b). Dotted lines stand for Ap (black lines, curve c) and ApCOO⁻ (10%) (red lines, curve d) corresponding derivative curves.

The XPS survey spectra of Ap and ApCOO⁻ (10%) depict the main lines for Ca, O, C, and P, as shown in the Supplementary Material under the title "XPS". Considering the experimental sensitivity factors relative to the different elements, surface stoichiometric ratios of $Ca_1P_{0.6}O_{2.8}$ and $Ca_1P_{0.55}O_{2.7}$ were determined for Ap and ApCOO⁻ (10%), respectively. The Ca:P ratio of Ap is in line with the expected theoretical hydroxyapatite stoichiometric ratio $Ca_1P_{0.6}O_{2.6}$ [35], while that of ApCOO⁻ (10%) is *ca.* 10% higher thus suggesting a slightly Ca-enriched surface.

XPS signals for the individual elements are also shown in the Supplementary Material under the title "XPS". Both, Ap and ApCOO⁻ (10%) powders show Ca2p1/2 and Ca2p3/2 lines at 347.0 eV separated by 3.5 eV, and P2p1/2 and P2p3/2 lines at 133 eV separated by 0.9 eV, characteristic of the apatite moieties. O1s XPS signals for Ap and ApCOO⁻ (10%) show the major contribution (> 98%) of a band at 531.5 eV assigned to oxygen atoms in phosphates [36]. Because O1s peaks tend to be broad and the binding energy of the surface groups of interest fall within a very narrow range, it is not possible to unambiguously discriminate organic oxygen contribution. However, despite organic contamination may mask the analysis of the C1s peak, O-C=O components appear at 288.5 eV and may be easily identified. The C1s peak of ApCOO⁻ (10%) clearly shows a higher contribution of carboxylates (*ca.* 21% of total C) than Ap (< 7%), thus also supporting the presence of surface propionic acid groups in the ApCOO⁻ (10%) samples.

Similar specific surface areas of (66.3 ± 0.1) and (67.5 ± 0.1) $m^2\ g^{-1}$ were determined from the fitting to the BET model of Ap and ApCOO⁻ (10%) N_2-adsorption isotherms, respectively.

3.2. ApCOOFu and ApCOOTy characterization

The ATR-IR spectrum of ApCOOFu and ApCOOTy depicted in Figure 5A curves a and b, respectively, show peaks at 2930-2840, 1595, 1440-1420, 1320, and 800 cm^{-1} already attributed to the presence of P-bonded propionate groups on the Ap surface. The spectrum of ApCOOFu also shows well defined peaks at 1320 and 760 cm^{-1} due to aromatic C-N and C-H bending and ring torsion, respectively, observed in Fu spectrum. Peaks at 1600 and 1560 cm^{-1}, characteristic of CO and NH bend in amides, may be assigned to the amide bonds linking propionic acid carboxylic groups with Fu amines. On the other hand, ApCOOTy shows peaks appearing at 1212, 1670-1630, and 1150 cm^{-1}, characteristic of stretching vibrations of C-O in phenols, C=O in amides, C-C in aromatic rings, and C-O in aliphatic esters and carboxylic acids, respectively, in line with the attachment of Ty through amide bonds to the carboxyl groups of $ApCOO^-$ (10%).

TGA curves of ApCOOFu powders (Figure 5B) show ~11% total mass loss between 150 and 550°C, assigned to the loss of surface bound organic matter (propionic acid and Fu) and lattice water. Around 4% mass Fu is estimated from the difference in mass loss between $ApCOO^-$ (10%) and ApCOOFu in that temperature range. Thus, *ca.* 0.013 moles Fu/100 g particles is estimated, almost one fourth that of attached propionic acid groups. ApCOOFu positive surface charge ($\varsigma = +2.8 \pm 0.1$, Zeta potential at pH 6.6 and 0.05 M ionic strength) compared to that of $ApCOO^-$ (10%) ($\varsigma = -21 \pm 2$) strongly suggest an efficient grafting of one of Fu amine groups to $ApCOO^-$ (10%) surface carboxyl, leaving the second Fu amine group free and protonated at pH 6.6 (Figure 1).

TGA curves of ApCOOTy, (Figure 5B), show an overall mass loss of 19% between 150 to 640°C, indicating that *ca.* 12% mass of Ty (0.042 moles, 75% that of surface carboxylates) is attached to 100 g of particles, thus supporting an efficient coverage with Ty.

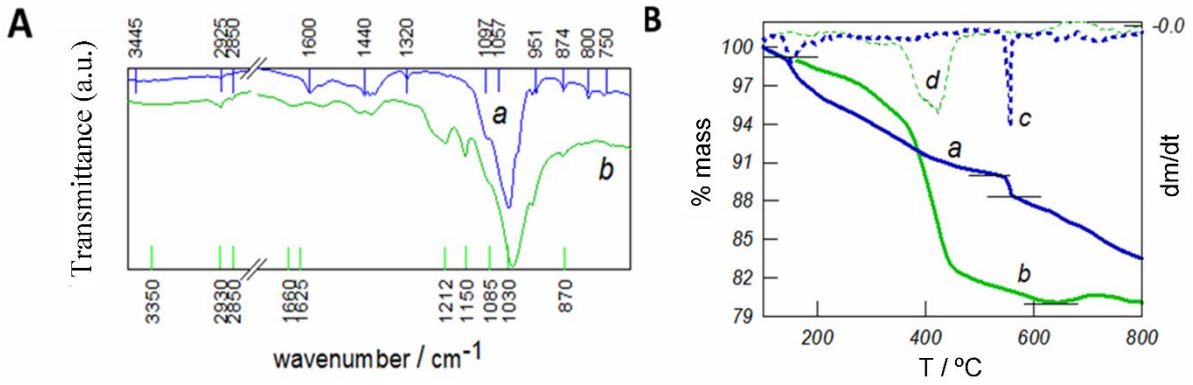

Figure 5. (A) ATR-IR spectra of ApCOOFu (blue lines, curve a), and ApCOOTy (green lines, curve b). (B) TGA performed in oxygen atmosphere of ApCOOFu (blue lines, curve a), ApCOOTy (green lines, curve b). Dotted lines stand for ApCOOFu (blue lines, curve c) and ApCOOTy (green lines, curve d) corresponding derivative curves.

Zeta potential values ($\varsigma = -15.2 \pm 0.5$) of ApCOOTy in aqueous suspensions of pH 6.6 and 0.05 M ionic strength compared to that of $ApCOO^-$ (10%) under identical conditions, *vide supra*, further supports the formation of peptide bonds between $ApCOO^-$ (10%) surface carboxyl groups and the amino group of Ty. Interestingly, ς values measured for physisorbed Ty on Ap (prepared in a way similar to ApCOOTy, but using Ap and Ty, without DCC/NHS) are $+2.76 \pm 0.08$, in agreement with literature reports suggesting that the α-carboxylate of the amino acid is preferentially bound to the apatite structure leading to positive surface charge [19]. Thus, these results support chemical linkage of Ty to the carboxylate-functionalized Ap surface *via* amide bonding.

3.3. BSA loading to Ap and $ApCOO^-$ (10%)

Since surface chemistry has great effects on protein adsorption, BSA loading and releasing on $ApCOO^-$ (10%) and Ap at 37ºC were investigated

and compared. Figure 6A shows the time-dependent adsorption of BSA on both, Ap and ApCOO⁻ (10%) at two initial solution concentrations, $[BSA]_0$ = 0.05 and 0.6 g L^{-1}, respectively. In the presence of low $[BSA]_0$, both, Ap and ApCOO⁻ (10%) rapidly adsorb BSA reaching similar loads after 5 h, in agreement with literature reports on BSA adsorption on hydroxyapatite crystallites [38]. A tenfold increase in $[BSA]_0$ leads, in both cases, to an early fast adsorption and a subsequent slower process. While the early fast regime is attributed to the surface acting as a sink to the proteins due to strong attractions, the sharp slowdown after a certain amount of protein adsorption is attributed to potential barrier crossing caused by the already adsorbed proteins [39].

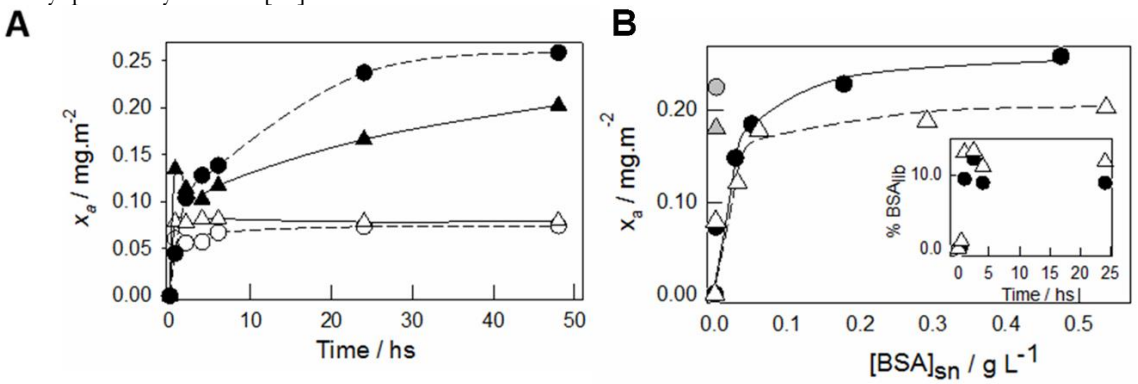

Figure 6. (A) Adsorption of BSA (x_a mg protein per m² of particle area) on Ap (circles) and ApCOO⁻ (10%) (triangles) as a function of time for initial protein concentrations $[BSA]_0$ = 0.05 (opened symbols) and 0.6 g L^{-1} (closed symbols) in aqueous solutions of pH 6.6-6.7 at 37 ºC. (B) Plot of the adsorbed BSA (x_a) vs. the BSA solution concentration, $[BSA]_{sn}$, at 37 ºC onto Ap (●) and ApCOO⁻ (10%) (Δ), respectively. Full and dashed lines stand for the fitting to eq. 1. Grey symbols stand for the values obtained from the desorption experiments shown in the inset. Inset B: %BSA desorption in phosphate buffer of pH 7.3 from a BSA load of 0.25 mg m^{-2} for Ap (●) and 0.20 mg m^{-2} for ApCOO⁻ (10%) (Δ), respectively, as a function of time.

Figure 6B shows Ap and ApCOO⁻ (10%) adsorption isotherms, where x_a is the amount of adsorbed BSA per unit surface area of substrate and $[BSA]_{sn}$ is the remaining BSA concentration in solution after no more protein is absorbed in the time-dependent adsorption experiments. Protein desorption experiments (Figure 6B inset) performed for the highest BSA loads investigated (0.25 mg m^{-2} Ap and 0.20 mg m^{-2} ApCOO⁻ (10%)) indicate that *ca.* 10% desorption takes place after three hours leading to new x_a and $[BSA]_{sn}$ values (grey symbols in Figure 5B). These values do not match those of the adsorption isotherm even in the presence of competitively adsorbed inorganic phosphates, in line with an irreversible BSA adsorption [38]. The experimental points of the respective isotherms can be reasonably fitted (r^2> 0.95) to a Langmuir-type form of isotherm given by eq. 1, where x_m stands for the saturation mass of BSA capable of covering 1 m² of the particles surface, and K is a constant related to the adsorption affinity.

$$x_a = \frac{K \cdot x_m \cdot [BSA]_{sn}}{1 + K \cdot [BSA]_{sn}} \quad (1)$$

From the fitting of the data in Figure 6B to eq. 1, x_m = (0.27 ± 0.05) mg m^{-2} and (0.21 ± 0.04) mg m^{-2} are obtained for Ap and ApCOO⁻ (10%), respectively, within the range reported for negatively charged hydroxyapatite surfaces at 37°C, either as obtained or amino acid-coated [7]. The low internal stability of BSA allowing the protein to expose its NH_3^+ groups on reaching the negatively charged surface has been reported to enhance BSA binding in surfaces of negative Z-potentials [40–44].

3.4. ApCOOFu and ApCOOTy optical properties

Ethanol suspensions of ApCOOFu of *ca.* 0.1 attenuation and Fu ethanol solutions of 0.1 absorbance, both at 510 nm, show similar fluorescence spectra as shown in Figure 7A. However, the fwhm fluorescence band of

covalently bonded Fu in ApCOOFu is somewhat broader and of much higher intensity than free Fu in ethanol solutions, in agreement with the reported behavior of Fu in solid matrix media [45]. An intense red fluorescence is also observed by fluorescence microscopy of ApCOOFu powders deposited on a glass slide, as shown in the fluorescence image in Figure 7A inset.

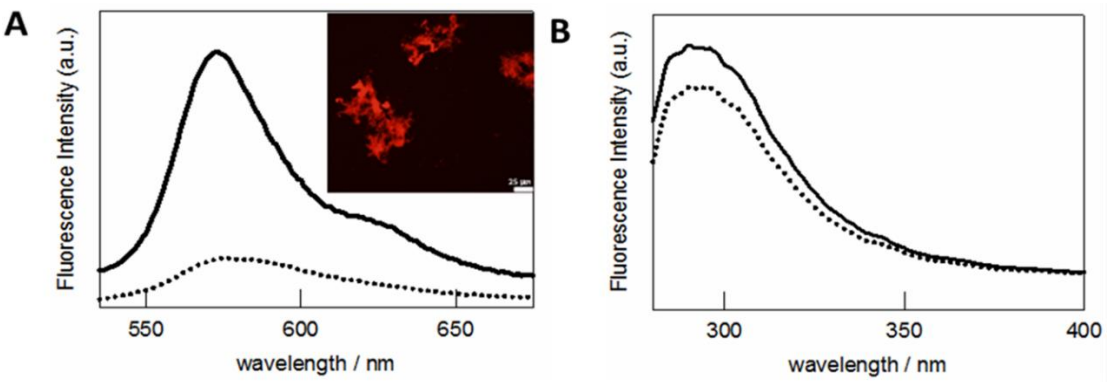

Figure 7. (A) Fluorescence spectra of an ethanol suspension of ApCOOFu (full line) and Fu solution in ethanol (dotted line) obtained upon excitation at 510 nm. Inset: Epifluorescence microscopy image of dried ApCOOFu powder on a glass slide. (B) ApCOOTy (full line) and Ty (dashed line) fluorescence spectra obtained upon excitation at 270 nm. The same attenuation/absorbance of *ca.* 0.1 at the corresponding excitation wavelengths was used in all cases.

It is well known from the literature [46-48], that the fluorescence quantum yield of triarylmethane dyes as Fu is higher in solid matrix than in liquid medium. The molecular rigidity of the dye in solid medium, together with conformational restrictions associated with the chemical linkage [49], appears to reduce the non-radiative relaxation processes that compete with fluorescence, and may explain the fluorescence increase observed here in ethanolic suspensions of ApCOOFu compared with the free dye.

ApCOOTy acetonitrile suspensions of *ca.* 0.1 attenuation and Ty acetonitrile solutions of 0.1 absorbance, both at 270 nm, show similar fluorescence spectra and fluorescence intensity, as shown in Figure 7B, supporting an efficient grafting of Ty to $ApCOO^-$ (10%).

3.5. Cytotoxicity evaluation

Cell viability of Ap and $ApCOO^-$ (10%) on Balb/C 3T3 cells after 24 h exposure was analyzed by microscopic images with AO staining [50]. Figure 8A shows the microscopic images of Balb/C 3T3 cells stained with AO grown on glass slides coated with Ap, and $ApCOO^-$ (10%) and on control glass without particle coating. Cell viability given as percentage of cell density with respect to the control shows a (42 ± 9)% ($p<0.001$) higher proliferation for culture cells grown on $ApCOO^-$ (10%) than those grown on Ap surface. A lower cell proliferation than controls is also reported in the literature for bare Ap, in line with the behavior observed here for Ap [51-53]. Reported *in vitro* assays with MC3T3-E1 osteoblast cell cultures and apatite surfaces [52,53] suggest that cells may be subject to changing levels of Ca^{2+} and PO_4^{3-} ions due to a rapid "pull-down" of extracellular ions onto the "bare" apatite surface. Thus, apatite coating with serum proteins is critical in making less detrimental the mediation of cell–apatite interaction, possibly through the modulation of phosphate-mediated cell death. Also, adsorption of bisphonates like tiludronate on bare apatite surfaces [53] is reported to stimulate preosteoblastic HOPs and HBMSCs cell proliferation. Our results showing higher proliferation for Balb/C 3T3 cells grown on $ApCOO^-$ (10%) than on "bare" Ap are in line with these observations, thus suggesting an increment in cell viability in $ApCOO^-$ (10%) microenvironment.

Cell viability of Ap and $ApCOO^-$ (10%) on Balb/C 3T3 cells after 24 h exposure was also analyzed by the MTT assay, measuring the reduction of MTT to formazan by dehydrogenase enzymes of intact mitochondria in living cells [54]. Figure 8B revealed *ca.* 15% increase ($p<0.001$) of mitochondrial activity for Ap with respect to the control (cells without treatment), while no

significant differences were observed for ApCOO⁻ (10%).

The fact that bare-apatite nanoparticles show less cell proliferation on Ap-deposited glasses than controls, while observing an enhanced proliferation than controls by MTT assays, may be assigned to a different surface distribution of the particles due to the composition of the supporting material (glass or plastic). Also, it is reported in the literature that assays directly counting viable cells are more sensitive than MTT as a test for the antiproliferative effect of hydroxyapatite [55]. Despite these differences, both viability assays seem to indicate that the use of PPA for the surface modification of Ap does not bring into negative effects towards Balb/C 3T3 cells.

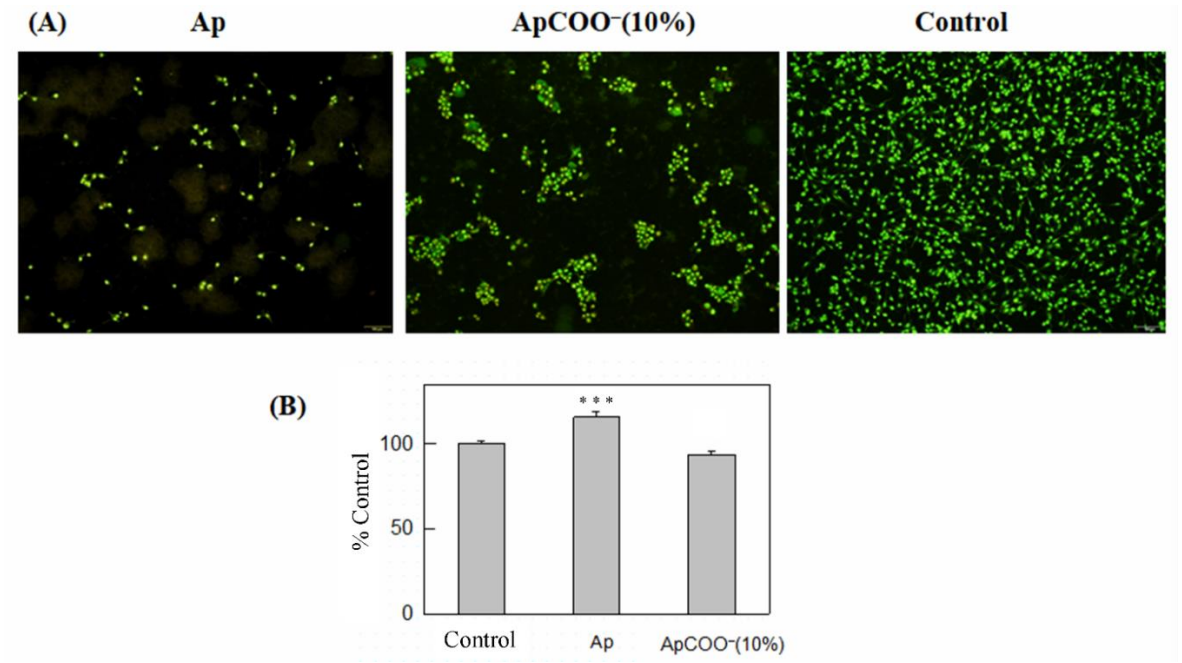

Figure 8. (A) Microscopic images of Balb/C 3T3 cells stained with AO grown on glass slides covered with Ap, ApCOO⁻ (10%), and control, respectively, after 24 h incubation. (B) MTT assays on Balb/C 3T3 cells after 24 h exposure to 0.53 mg Ap and ApCOO⁻ (10%). *** indicate significant differences at $p < 0.001$ with respect to the controls.

4. Conclusions

Herein we describe the one pot synthesis of modified Ap by surface grafting of organophosphonic acids involving P-O-P bonds and yielding propionic acid-terminated Ap (ApCOO⁻). This new synthesis strategy was developed to increase apatite available surface groups for the covalent functionalization with (bio)molecules of interest. The estimated coverage of a propionic acid group per 20 Å² and the observed surface charge inversion of the coated apatite strongly suggest an efficient organophosphonic surface grafting. The obtained particles do not show additional cytotoxic effects on surface functionalization towards Balb/C 3T3 cells.

ApCOO⁻ abundant carboxyl surface groups facilitated the efficient particles grafting with Fu and Ty involving stable amide bonds. These new material hybrids showed particular properties with potential technological uses: ApCOOFu is a highly fluorescent apatite (510 nm maximum excitation, 570-650 nm emission) suitable for optical sensing purposes; ApCOOTy is a highly stable, negatively-charged aminoacid-covered apatite whose potential properties as filling material in bone tissue engineering needs still being explored. Moreover, a similar grafting strategy may be used to incorporate other bioactive molecules to the Ap surface, such as osteogenic-related peptides, to produce peptide-modified composites with enhanced functions as bone repair materials [56]. Irrespective of these particular examples, it was demonstrated that ApCOO⁻ might constitutes a versatile platform suitable for bone tissue engineering.

Supplementary information

List of Materials, Standarized equipment and procedures, Biological standard procedures: Cell cultures and Cell viability assays (AO staining and MTT assay), XPS survey and P2p, Ca2p, O1s, and C1s signals, SEM-EDS spectra and ApCOOFu colored filtrates are available in the Supplementary Material.

Funding

This research was funded by ANPCyT, grants PICT 2014-2746, 2014-2153, and 2015-1266. Financial support for academic interchange by the European Union (Horizon 2020 research and innovation program under the Marie Skłodowska - Curie grant, agreement No 645551) is acknowledged.

Acknowledgments

M.L.D. thanks CONICET, Argentina, for a graduate studentship. M.C.G. and H.B.R. are research members of CONICET.

Conflicts of Interest

The authors declare no conflict of interest.

References

1. Singh, G.; Singh, R.P.; Jolly, S.S. Customized hydroxyapatites for bone-tissue engineering and drug delivery applications: a review. *J. Sol-Gel Sci. Technol.* **2020**, in press. https://doi.org/10.1007/s10971-020-05222-1

2. Molino, G.; Palmieri, M.C.; Montalbano, G.; Fiorilli, S.; Vitale-Brovarone, C. Biomimetic and mesoporous nano-hydroxyapatite for bone tissue application: a short review. *Biomed. Mater.* **2020**, *15*, 022001. https://doi.org/10.1088/1748-605X/ab5f1a

3. Mondal, S.; Dorozhkin, S.V.; Pal, U. Recent progress on fabrication and drug delivery applications of nanostructured hydroxyapatite. *WIREs Nanomed. Nanobiotechnol.* **2018**, *10*, e1504. https://doi.org/10.1002/wnan.1504

4. Palmer, L.C.; Newcomb, C.J.; Kaltz, S.R.; Spoerke, E.D.; Stupp, S.I. Biomimetic systems for hydroxyapatite mineralization inspired by bone and enamel. *Chem. Rev.* **2008**, *108*, 4754-4783. https://doi.org/10.1021/cr8004422

5. Lee, W.-H.; Loo, C.-Y.; Rohanizadeh, R. A review of chemical surface modification of bioceramics: Effects on protein adsorption and cellular response. *Colloids Surf. B Biointerfaces* **2014**, *122*, 823-834. https://doi.org/10.1016/j.colsurfb.2014.07.029

6. Dorozhkin, S.V. Functionalized calcium orthophosphates ($CaPO_4$) and their biomedical applications. *J. Mater. Chem. B* **2019**, *7*, 7471-7489. https://doi.org/10.1039/c9tb01976f

7. Lee, W.-H.; Loo, C.-Y.; Van, K.L.; Zavgorodniy, A.V.; Rohanizadeh, R. Modulating protein adsorption onto hydroxyapatite particles using different amino acid treatments. *J. R. Soc. Interface* **2012**, *9*, 918-927. https://doi.org/10.1098/rsif.2011.0586

8. Goonasekera, C.S.; Jack, K.S.; Cooper-White, J.J.; Grondahl, L. Attachment of poly(acrylic acid) to 3-aminopropyltriethoxysilane surface-modified hydroxyapatite. *J. Mater. Chem. B* **2013**, *1*, 5842-5852. https://doi.org/10.1039/C3TB21110J

9. D'Andrea, S.C.; Fadeev, A.Y. Covalent Surface Modification of Calcium Hydroxyapatite Using n-Alkyl- and n-Fluoroalkylphosphonic Acids. *Langmuir* **2003**, *19*, 7904-7910. https://doi.org/10.1021/la027000s

10. El-Hammari, L.; Marroun, H.; Laghzizil, A.; Saoiabi, A.; Roux, C.; Livage, J.; Coradin, T. Organically modified porous hydroxyapatites: A comparison between alkylphosphonate grafting and citrate chelation. *J. Solid State Chem.* **2008**, *181*, 848-854. https://doi.org/10.1016/j.jssc.2008.01.030

11. Boanini, E.; Torricelli, P.; Boga, C.; Micheletti, G.; Cassani, M.C.; Fini, M.; Bigi, A. (9R)-9-Hydroxystearate-Functionalized Hydroxyapatite as Antiproliferative and Cytotoxic Agent toward Osteosarcoma Cells. *Langmuir* **2016**, *32*, 188-194. https://doi.org/10.1021/acs.langmuir.5b03754

12. Amjad, Z. The Influence of Polyphosphates, Phosphonates, and Poly (carboxy1ic acids) on the Crystal Growth of Hydroxyapatite. *Langmuir* **1987**, *3*, 1063-1069. https://doi.org/10.1021/la00078a032

13. Ishihara, S.; Matsumoto, T.; Onoki, T.; Uddin, M.H.; Sohmura, T.; Nakahira, A. Regulation of the protein-loading capacity of hydroxyapatite by mercaptosuccinic acid modification. *Acta Biomater.* **2010**, *6*, 830-835. https://doi.org/10.1016/j.actbio.2009.10.019

14. Yokoi, T.; Kawashita, M.; Ohtsuki, C. Biomimetic mineralization of calcium phosphates in polymeric hydrogels containing carboxyl groups. *J. Asian Ceram. Soc.*

2013, *1*, 155-162. https://doi.org/10.1016/j.jascer.2013.04.003

15. Hidzir, N.M.; Hill, D.J.T.; Martin, D; Grøndahl, L. *In vitro* mineralisation of grafted ePTFE membranes carrying carboxylate groups. *Bioactive Materials* **2017**, *2*, 27e3428. https://doi.org/10.1016/j.bioactmat.2017.02.002

16. Valeur, E.; Bradley, M. Amide bond formation: beyond the myth of coupling reagents. *Chem. Soc. Rev.* **2009**, *38*, 606-631. https://doi.org/10.1039/b701677h

17. Sawyer, A.A.; Hennessy, K.M.; Bellis, S.L. Regulation of mesenchymal stem cell attachment and spreading on hydroxyapatite by RGD peptides and adsorbed serum proteins. *Biomaterials* **2005**, *26*, 1467-1475. https://doi.org/10.1016/j.biomaterials.2004.05.008

18. Costa, D.; Savio, L.; Pradier, C.M. Adsorption of Amino Acids and Peptides on Metal and Oxide Surfaces in Water Environment: A Synthetic and Prospective Review. *J. Phys. Chem. B* **2016**, *120*, 7039-7052. https://doi.org/10.1021/acs.jpcb.6b05954

19. Gonzalez-McQuire, R.; Chane-Ching, J.-Y.; Vignaud, E.; Lebuglec, A.; Mann, S. Synthesis and characterization of amino acid-functionalized hydroxyapatite nanorods. *J. Mater. Chem.* **2004**, *14*, 2277-2281. https://doi.org/10.1039/b400317a

20. Kataoka, T.; Samitsu, S.; Okuda, M.; Kawagoe, D.; Tagaya, M. Highly Luminescent Hydroxyapatite Nanoparticles Hybridized with Citric Acid for Their Bifunctional Cell-Labeling and Cytostatic Suppression Properties. *ACS Appl. Nano Mater.* **2020**, *3*, 241-256. https://doi.org/10.1021/acsanm.9b01933

21. Kumar Khajuria, D.; Bhooshan Kumar, V.; Gigi, D.; Gedanken, A.; Karasik, D. Accelerated Bone Regeneration by Nitrogen-Doped Carbon Dots Functionalized with Hydroxyapatite Nanoparticles. *ACS Appl. Mater. Interfaces* **2018**, *10*, 19373-19385. https://doi.org/10.1021/acsami.8b02792

22. Mondal, S.; Dorozhkin, S.V.; Pal, U. Recent progress on fabrication and drug delivery applications of nanostructured hydroxyapatite. *WIREs Nanomed. Nanobiotechnol.* **2018**, *10*, e1504. https://doi.org/10.1002/wnan.1504

23. Lee, J.; Ju, M.; Cho, O.H.; Kim, Y.; Nam, K.T. Tyrosine-Rich Peptides as a Platform for Assembly and Material Synthesis. *Adv. Sci.* **2019**, *6*, 1801255. https://doi.org/10.1002/advs.201801255

24. Viswanatha, V.; Hruby, V.J. Conversion of L-tyrosine to L-phenylalanine. Preparation of L-[3',5'-13C2]phenylalanine. *J. Org. Chem.* **1980**, *45*, 2010-2012. https://doi.org/10.1021/jo01298a055

25. Jensen, E.; Bundgaard, H. Peptide esters as water-soluble prodrugs for hydroxyl containing agents: Chemical stability and enzymatic hydrolysis of benzyl esters of glycine, diglycine and triglycine. *Int. J. Pharm.* **1991**, *71*, 117-125. https://doi.org/10.1016/0378-5173(91)90073-W

26. Wang, Z.; Xu, Z.; Zhao, W.; Sahai, N. A Potential Mechanism for Amino Acid-Controlled Crystal Growth of Hydroxyapatite. *J. Mater. Chem. B* **2015**, *3*, 9157-9167. https://doi.org/10.1039/C5TB01036E

27. Ruiz-Mendoza, S.C.; Moreno-Aldana, L.C.; Delgado-Mejía, E. A bridged acid-base wet-milling synthesis of high purity hydroxyapatite. *Mater. Res.* **2008**, *11*, 187-192. https://doi.org/10.1590/S1516-14392008000200013

28. Prevéy, P.S. X-Ray Diffraction Characterization of Crystallinity and Phase Composition in Plasma-Sprayed Hydroxyapatite Coatings. *J. Therm. Spray Technol.* **2000**, *9*, 369-376. https://doi.org/10.1361/105996300770349827

29. Liao, C.J.; Lin, F.H.; Chen, K.S.; Sun, J.S. Thermal decomposition and reconstitution of hydroxyapatite in air atmosphere. *Biomaterials* **1999**, *20*, 1807-1813. https://doi.org/10.1016/S0142-9612(99)00076-9

30. Figueiredo, M.M.; Gamelas, J.A.F.; Martins, A.G. Characterization of bone and bone-based graft materials using FTIR spectroscopy. In *Infrared Spectroscopy – Life and Biomedical Sciences*; Theophanides, T., Ed.; InTech, Janeza Trdine 9, 51000 Rijeka, Croatia, 2012; pp. 315-338. https://doi.org/10.5772/36379

31. Ibrahim, M.; Nada, A.; Kamal, D.E. Density functional theory and FTIR spectroscopic study of carboxyl group. *Indian J. Pure Appl. Phys.* **2005**, *43*, 911-917. http://nopr.niscair.res.in/handle/123456789/8906

32. NIST Chemistry WebBook: NIST Standard Reference Database Number 69. National Institute of Standards and Technology, Gaithersburg, MD 20899, 2000. https://doi.org/10.18434/T4D303 (accessed November 12, 2015).

33. Sun, L.; Chow, L.C.; Frukhtbeyn, S.A.; Bonevich, J.E. Preparation and Properties of Nanoparticles of Calcium Phosphates With Various Ca/P Ratios. *J. Res. Natl. Inst. Stand. Technol.* **2010**, *115*, 243-255. https://doi.org/10.6028/jres.115.018

34. Janietz, D. Chapter 7: Liquid Crystals at Interfaces. In *Handbook of Surfaces and Interfaces of Materials, Vol. 1, Surface and Interface Phenomena*; Nalwa, H.S., Ed.; Academic Press, San Diego, USA, 2001; pp. 423-446. https://doi.org/10.1016/B978-012513910-6/50014-1

35. Rey, C.; Combes, C.; Drouet, C.; Grossin, D. 1.111 – Bioactive Ceramics: Physical Chemistry. In *Comprehensive Biomaterials, Vol. 1*; Ducheyne, P., Ed.;

Elsevier, Amsterdam, the Netherlands, 2011; pp. 187-281. https://doi.org/10.1016/B978-0-08-055294-1.00178-1

36. NIST X-ray Photoelectron Spectroscopy Database: NIST Standard Reference Database 20. National Institute of Standards and Technology, Gaithersburg, MD 20899, 2000. http://dx.doi.org/10.18434/T4T88K (accessed November 12, 2015).

37. Kandori, K.; Sawai, S.; Yamamoto, Y.; Saito, H.; Ishikawa, T. Adsorption of albumin on calcium hydroxylapatite. *Colloids and Surfaces* **1992**, *68*, 283-289. https://doi.org/10.1016/0166-6622(92)80214-M

38. Yin, G.; Liu, Z.; Zhan, J.; Ding, F.; Yuan, N. Impacts of the surface charge property on protein adsorption on hydroxyapatite. *Chem. Eng. J.* **2002**, *87*, 181-186. https://doi.org/10.1016/S1385-8947(01)00248-0

39. Fang, F.; Satulovsky, J.; Szleifer, I. Kinetics of protein adsorption and desorption on surfaces with grafted polymers. *Biophys. J.* **2005**, *89*, 1516-1533. https://doi.org/10.1529/biophysj.104.055079

40. Satzer, P.; Svec, F.; Sekot, G.; Jungbauer, A. Protein adsorption onto nanoparticles induces conformational changes: Particle size dependency, kinetics, and mechanisms. *Eng. Life Sci.* **2016**, *16*, 238-246. https://doi.org/10.1002/elsc.201500059

41. Hughes Wassell, D.T.; Hall, R.; Embery, G. Adsorption of bovine serum albumin onto hydroxyapatite. *Biomaterials* **1995**, *16*, 697-702. https://doi.org/10.1016/0142-9612(95)99697-K

42. Mura-Galelli, M.J.; Voegel, J.C.; Behr, S.; Bres, E.F.; Schaaf, P. Adsorption/desorption of human serum albumin on hydroxyapatite: a critical analysis of the Langmuir model. *Proc. Natl. Acad. Sci. USA* **1991**, *88*, 5557-5561. https://doi.org/10.1073/pnas.88.13.5557

43. Meder, F.; Daberkow, T.; Treccani, L.; Wilhelm, M.; Schowalter, M.; Rosenauer, A.; Mädler, L.; Rezwan, K. Protein adsorption on colloidal alumina particles functionalized with amino, carboxyl, sulfonate and phosphate groups. *Acta Biomater.* **2012**, *8*, 1221-1229. https://doi.org/10.1016/j.actbio.2011.09.014

44. Hu, X.N.; Yang, B.C. Conformation change of bovine serum albumin induced by bioactive titanium metals and its effects on cell behaviors. *J. Biomed. Mater. Res. - Part A* **2014**, *102*, 1053-1062. https://doi.org/10.1002/jbm.a.34768

45. Pathrose, B.; Nampoori, V.P.N.; Radhakrishnan, P.; Mujeeb, A. Measurement of Absolute Fluorescence Quantum Yield of Basic Fuchsin Solution Using a Dual-Beam Thermal Lens Technique. *J. Fluoresc.* **2014**, *24*, 895-898. https://doi.org/10.1007/s10895-014-1369-0

46. Duxbury, D.F. The photochemistry and photophysics of triphenylmethane dyes in solid and liquid media. *Chem. Rev.* **1993**, *93*, 381-433. https://doi.org/10.1021/cr00017a018

47. Baptista, M.S.; Indig, G.L. Effect of BSA Binding on Photophysical and Photochemical Properties of Triarylmethane Dyes. *J. Phys. Chem. B* **1998**, *102*, 4678-4688. https://doi.org/10.1021/jp981185n

48. Vinitha, G.; Ramalingam, A. Third-order optical nonlinearities and optical-limiting properties of a Pararosanilin dye in liquid and solid media. *Laser Phys.* **2008**, *18*, 1070-1073. https://doi.org/10.1134/S1054660X08090120

49. Mondal, S.; Verma, A; Saha, S. Conformationally Restricted Triarylmethanes: Synthesis, Photophysical Studies, and Applications. *Eur. J. Org. Chem.* **2019**, *2019*, 864-894. https://doi.org/10.1002/ejoc.201800971

50. Hayashi, M.; Sofuni, T.; Ishidate, M. An application of Acridine Orange fluorescent staining to the micronucleus test. *Mutat. Res. Lett.* **1983**, *120*, 241-247. https://doi.org/10.1016/0165-7992(83)90096-9

51. Shi, Z.; Huang, X.; Cai, Y.; Tang, R.; Yang, D. Size effect of hydroxyapatite nanoparticles on proliferation and apoptosis of osteoblast-like cells. *Acta Biomater.* **2009**, *5*, 338-345. https://doi.org/10.1016/j.actbio.2008.07.023

52. Tsang, E.J.; Arakawa, C.K.; Zuk, P.A.; Wu, B.M. Osteoblast interactions within a biomimetic apatite microenvironment. *Ann. Biomed. Eng.* **2011**, *39*, 1186-1200. https://doi.org/10.1007/s10439-010-0245-6

53. Pascaud, P.; Bareille, R.; Bourget, C.; Amédée, J.; Rey, C.; Sarda, S. Interaction between a bisphosphonate, tiludronate and nanocrystalline apatite: in vitro viability and proliferation of HOP and HBMSC cells. *Biomed. Mater.* **2012**, *7*, 54108. https://doi.org/10.1088/1748-6041/7/5/054108

54. Mosmann, T. Rapid colorimetric assay for cellular growth and survival: Application to proliferation and cytotoxicity assays. *J. Immunol. Methods* **1983**, *65*, 55-63. https://doi.org/10.1016/0022-1759(83)90303-4

55. Theiszová, M.; Jantová, S.; Dragúnová, J.; Grznárová, P.; Palou, M. Comparison the cytotoxicity of hydroxyapatite measured by direct cell counting and MTT test in murine fibroblast NIH-3T3 cells. *Biomed. Pap. Med. Fac. Univ. Palacky Olomouc Czech Repub.* **2005**, *149*, 393-396. https://doi.org/10.5507/bp.2005.066

56. Wang, C.; Liu, Y.; Fan , Y.; Li, X. The use of bioactive peptides to modify materials for bone tissue repair. *Regen. Biomater.* **2017**, *4*, 191-206. https://doi.org/10.1093/rb/rbx011

Supplementary Material

1. Materials

$Ca(OH)_2$ 98.5 wt% (Biopack), and phosphoric acid 85%, 3-phosphonopropionic acid (PPA), N,N´-dicyclohexylcarbodiimide (DCC), N-hydroxysuccinimide (NHS), 4-[(4-aminophenyl)-(4-iminocyclohexa-2,5-dien-1-ylidene)methyl]aniline hydrochloride (basic fuchsin (Fu), purity >95%), and ethanol, all from Sigma Aldrich, were used without further purification. Deionized water was Milli-Q purified (18.2 MΩcm and < 6 ppb TOC). Different KH_2PO_4 / K_2HPO_4 (Merck) phosphate buffered solutions (PBS) of 0.1 M ionic strength were used. Acetonitrile was from Merck. Coumasie Brillant Blue G250 (Sigma) was used for BSA (BSA) quantification.

Tyrosine (Ty) benzyl ester was obtained in the laboratory. To that purpose, 1.5 g of L-Ty was mixed with 4 mL of concentrated HCl and 40 mL benzyl alcohol and the resulting solution maintained at 81 ºC for *ca.* one hour before product extraction with ethyl ether and 10% HCl aqueous solutions. The pH of the remaining aqueous phase was adjusted to 9.1 by NH_4OH addition. The precipitated Ty benzyl ester solid was isolated by filtration with 0.22 μm hydrophilic membranes and washed with ethanol.

2. $ApCOO^-$ Stability

Aqueous suspensions of $ApCOO^-$ (10%) were left at 40 ºC for 48 h, filtered with 0.4 μm membranes and the pH and absorbance of the liquid filtrate were measured, taking pure Ap filtrates with equal treatment as absorption blanks. The pH remained constant to 6.7 as well as the absorbance at 300 nm. Moreover, absorbance spectrum of the liquid filtrate resembles that of pure hydroxyapatite filtrates, and assigned to the light dispersion of small apatite particles, as shown in Figure S1. These observations strongly support a high stability towards PPA elimination from the apatite surface.

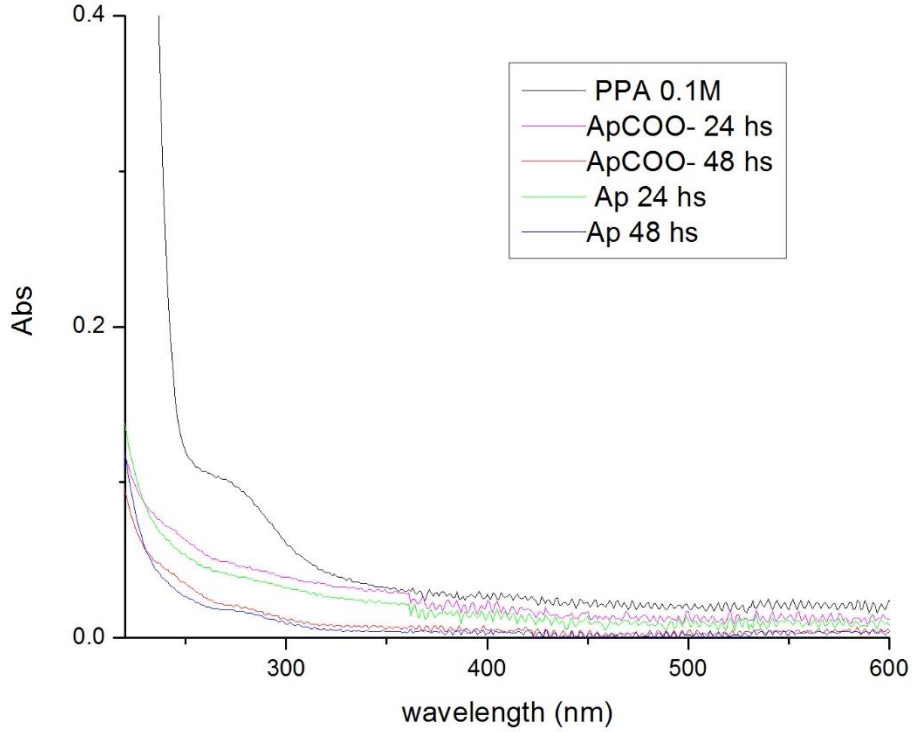

Figure S1. Absorbance spectrum of the liquid filtrate of $ApCOO^-$ (10%) suspensions stored for different times, as compared to those of Ap suspensions and a pure aqueous solution of PPA.

3. ApCOOFu coloured filtrates

ApCOOFu can be separated from its ethanolic suspensions by filtration with 0.22 μm filters, as observed by the red solid retained on the filter after thorough washing with ethanol. Contrary to this observations, free Fu is not adsorbed on the membrane, neither on ApCOO⁻ (10%) after thorough washing, as shown in Figure S2.

Figure S2. Solid filtrate retained in the membrane for (from left to right) Fu, Fu + ApCOO⁻ (10%), and ApCOOFu. Notice that the free dye in solution is not absorbed on the filter membrane, neither on ApCOO⁻ (10%), as it passes through the filter, while ApCOO⁻ (10%) is retained.

4. Equipment

The crystalline phase content of the samples was assessed by X-ray Diffraction (XRD) using a Philips X'pert equipped with a PW3710 control unit and a PW3020 vertical goniometer, Cu-Kα radiation, and a Ni filter and 40 kV-20mA.

High Resolution Transmission Electron Microscopy (HRTEM) micrographs were obtained with a FEI Talos F200X instrument equipped with a CCD camera. Samples were dry deposited on 200 mesh carbon-coated copper grids.

The functional groups present in the prepared nanoparticles were identified by their IR spectrum obtained with a Nicolet 380 spectrophotometer working at 64 scans with 4 cm^{-1} resolution in the overall range 4000-400 cm^{-1}. Samples were prepared by pressing a grounded mixture of 1% of the particles powder with 99% dry KBr at a load of 5 tons. For ATR-FTIR an accesory Pike MIRacle™ Single Reflection ATR Ge crystal was used.

The thermal behaviour of the powders in an oxygen environment was studied by thermal gravimetric analysis (TGA) using a Rigaku Serie Thermo Plus Evo instrument. The temperature program involved an initial temperature of 30 °C followed by a 10 °C /min ramp up to 1000 °C and maintained at this temperature for 10 minutes.

Nitrogen gas-volumetric adsorption experiments for specific surface area determinations (BET model) were performed at 77 K by means of a ASAP2020 by Micromeritics model. Before each measurement, samples were outgassed overnight at 80°C at a residual pressure of about 10^{-2} mbar to guarantee a good cleaning of the sample surface.

The X-ray photoelectron spectroscopy (XPS) spectra were obtained under UHV with a XR50 Specs GmbH spectrometer using Mg K(α) as the excitation source and a PHOIBOS 100 half sphere electron energy analyzer. A two-point calibration of the energy scale was performed using sputtered cleaned gold (Au 4f7/2, binding energy (BE) 84.00 eV) and copper (Cu 2p3/2, BE: 932.67 eV) samples. Internal calibration to correct for surface charging was performed with the C 1s peak at BE = 284.6 eV due to adventitious carbon. High resolution XPS spectra were taken to get a better insight into the chemical environment of the different atoms. A Shirley-type background from each spectrum was used to remove the effect of the extrinsic structure loss and the spectrum resolved by Gaussian-Lorentzian fitting, keeping χ^2 to their minimum values.

Electrophoretic mobility experiments were obtained at (25.0 ± 0.1)°C with a Malvern Zetasizer Nano ZS. Samples were adjusted to 0.01 M ionic strength with sodium perchlorate and pH 6.6 with sodium

hydroxide. Each sample was analyzed three times. However, due to the slow agglomeration of the particles, only the net sign of the surface charge is taken as reliable.

A microscope (Olympus BX51, Olympus Corp., Tokyo, Japan) equipped with DM500 dichroic mirrors and BP450-480 excitation and BA515 emission filters, connected to an Olympus DP71 (Olympus Corp., Tokyo, Japan) color video camera was used to characterize solid powders deposited on glass slides and to observe adherent cells stained with AO dye. The images were taken immediately after opening the microscope shutter to the computer monitor. Surface densities of cells were obtained from digital images using the Image-Pro Plus program. Each assay was repeated three times in independent experiments.

Steady-state fluorescence spectra were obtained on a PTI model QM-1 spectrofluorometer (London, Ontario, Canada), in a 1 cm path-length quartz cuvette (Hellma) at right angle. Measurements were performed at (25 ± 2)°C in air-saturated ethanol solutions/suspensions of Fu and ApCOOFu and acetonitrile solutions/suspensions of Ty and ApCOOTy. In order to reduce the distortions in emission measurements due to light scattering reaching the detector, particularly important in Ap suspensions, several cut-off optical filters in the excitation and emission paths were used. Particularly for Fu-containing samples excited in the 490-510 nm range with emission detected between 530 nm and 700 nm, a short-pass filter ASAHI XVS510 was used for excitation and a long-pass 2 mm thick filter Schott OG530 was used for emission. Samples containing Ty were excited at 270 nm and emission was registered in the 280-360 nm interval, using a long-pass 2 mm thick Schott WG280 filter for emission. In all cases, spectra were corrected for changes in the detector responsivity and filters transmittance with wavelength. All spectra were corrected for the wavelength-dependent sensitivity of the detector and the source. Additionally, the fluorescence spectra were corrected for Raman scattering by using the associated solvent emission spectrum.

SEM/EDS studies were performed using an Environmental Scanning Electron Microscope FEI ESEM Quanta 200 instrument, equipped with a tungsten filament emitter and working in the low vacuum mode (0.1 to 1 Torr), coupled to an EDS model EDAX SDD Apollo 40.

5. Loading of BSA

Bovine Serum Albumin (BSA) adsorption on Ap and $ApCOO^-$ (10%) was investigated in batch experiments. To that purpose, 10 mg of either Ap or $ApCOO^-$ (10%) were introduced in polypropylene tubes containing 10 mL of BSA solutions of concentrations in the range between 50 and 600 μg mL^{-1}. The mixture was allowed to stand between 24 and 48 h depending on the initial BSA concentrations, *vide infra*, at 37 ºC and under constant stirring. After that time, 1 mL of the aqueous phase was centrifuged at 900 rpm during 10 minutes and the supernatant proteins quantified by the Bradford method [Bradford, M. M. *Anal. Biochem.* **1976**, *72*, 248-254. https://doi.org/10.1016/0003-2697(76)90527-3]. To that purpose, around 500 to 40 μL of supernatant were mixed with 950 μL of coumasie blue G250 solution and the absorbance at 595 nm used to quantify BSA concentration in solution using a concentration–intensity calibration curve. The BSA loading amount per unit area, x_a, was calculated based on the depletion of BSA in the solution volume V and the total surface area of a mass of particles m used in the adsorption experiments, $x_a = ([BSA]_o - [BSA]_{sn}) \times V/(m \times A_{sp})$, with $[BSA]_o$ and $[BSA]_{sn}$, the initial and final BSA concentrations, respectively, and A_{sp} the specific surface area determined by the application of the BET model to N_2 adsorption isotherms.

For BSA release experiments, 10 mg of the highest BSA-loaded samples were incubated in 10 mL of phosphate buffer (Na_2HPO_4 1.6 g L^{-1}, KH_2PO_4 0.20 g L^{-1}, in NaCl 8.18 g L^{-1} and KCl 0.92 g L^{-1}). The mixture was allowed to stand for different periods of time at 37 ºC under constant stirring. After each time, the aqueous phase was removed, centrifuged at 900 rpm during 10 minutes, and the proteins in the supernatant quantified.

6. XPS

The XPS survey spectra of ApCOO⁻ (10%) shown in Figure S3(A) depicts the main lines for Ca, O, C, and P. Figures S3(B) and (C) show P2p1/2 and P2p3/2 lines at 133 eV separated by 0.9 eV (not resolved in the spectrum), and Ca2p1/2 and Ca2p3/2 lines at 347.0 eV separated by 3.5 eV, respectively, characteristic of the apatite moieties. Figure S3(E) shows C1s signals for Ap and ApCOO⁻ (10%). The C1s peak of ApCOO⁻ (10%) clearly shows a higher contribution of carboxylates (*ca.* 21% of total C) than in Ap (< 7%).

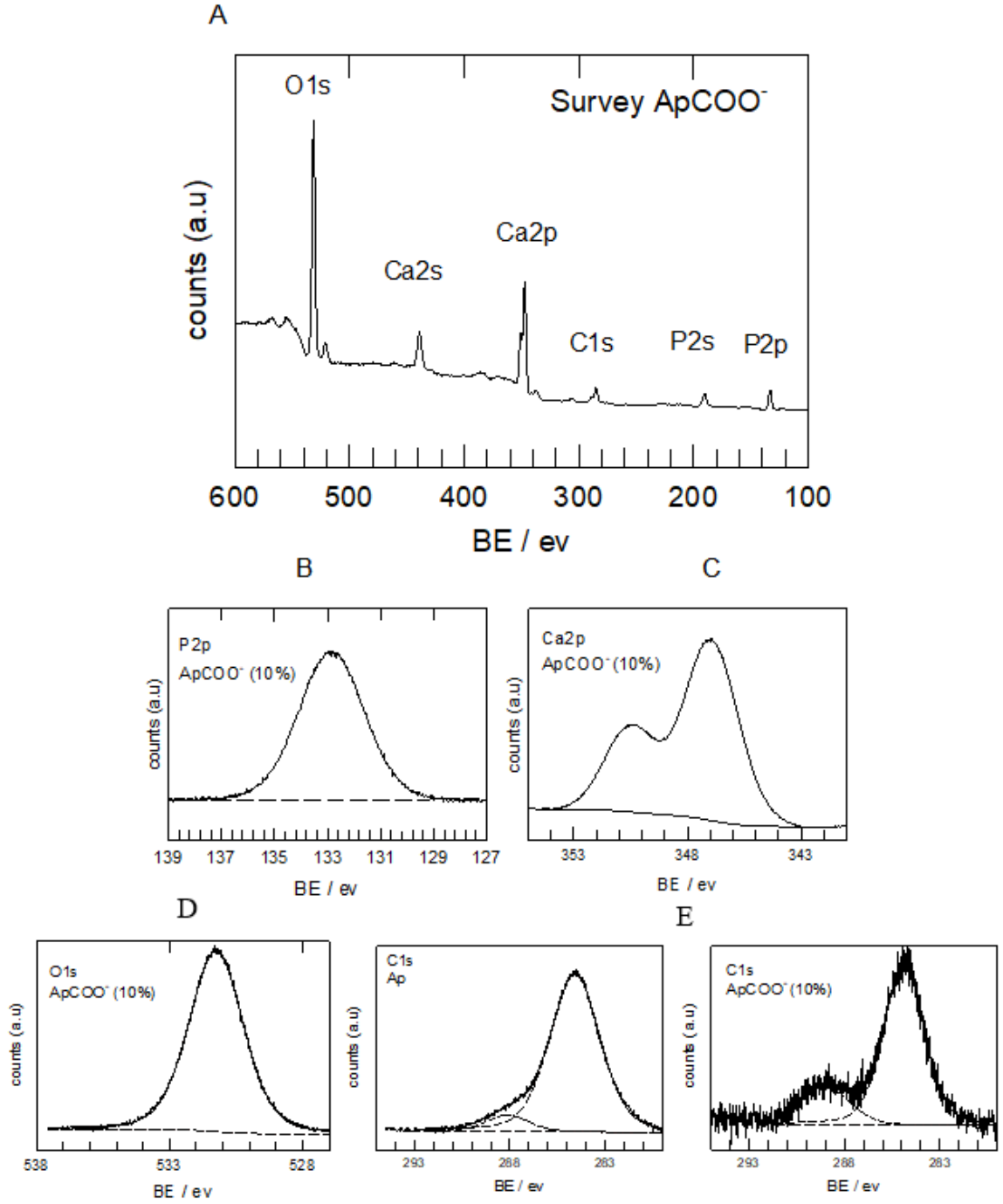

Figure S3. (A) XPS survey spectra, (B) P2p, (C) Ca2p, and (D) O1s XPS signals obtained for ApCOO⁻ (10%). (E) C1s XPS signals (full lines) and contributing peaks (dashed lines) observed for Ap and ApCOO⁻ (10%), respectively.

7. SEM-EDS

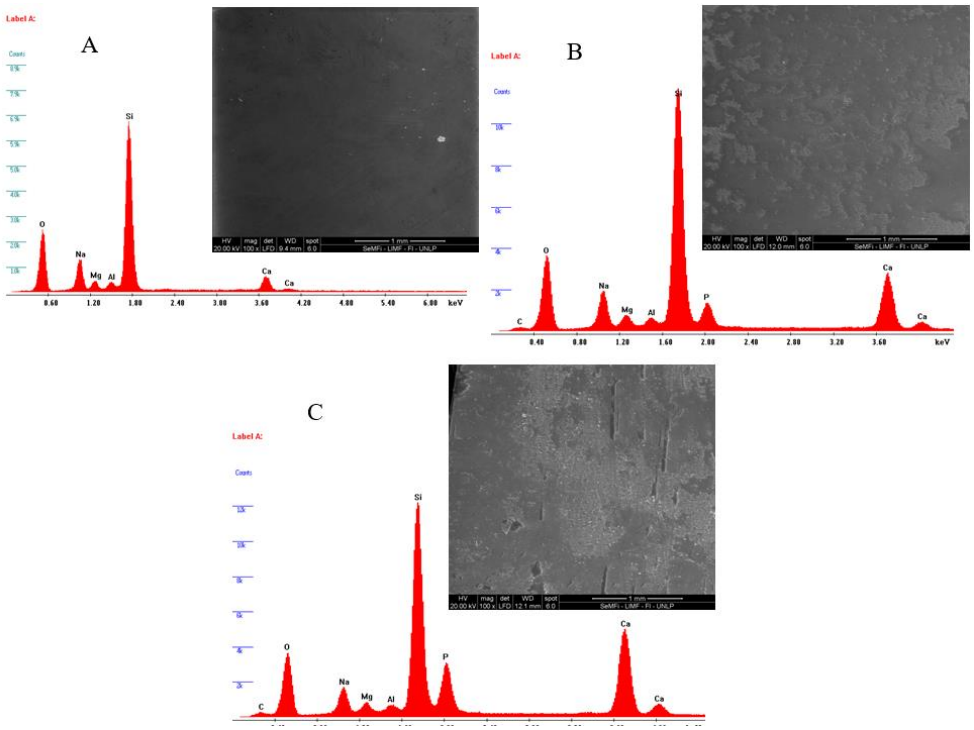

Figure S4. SEM images and EDS profiles of particle-covered glass slides before washing with PBS: (A) Glass slide without particles (control); (B) Ap; (C) ApCOO⁻ (10%).

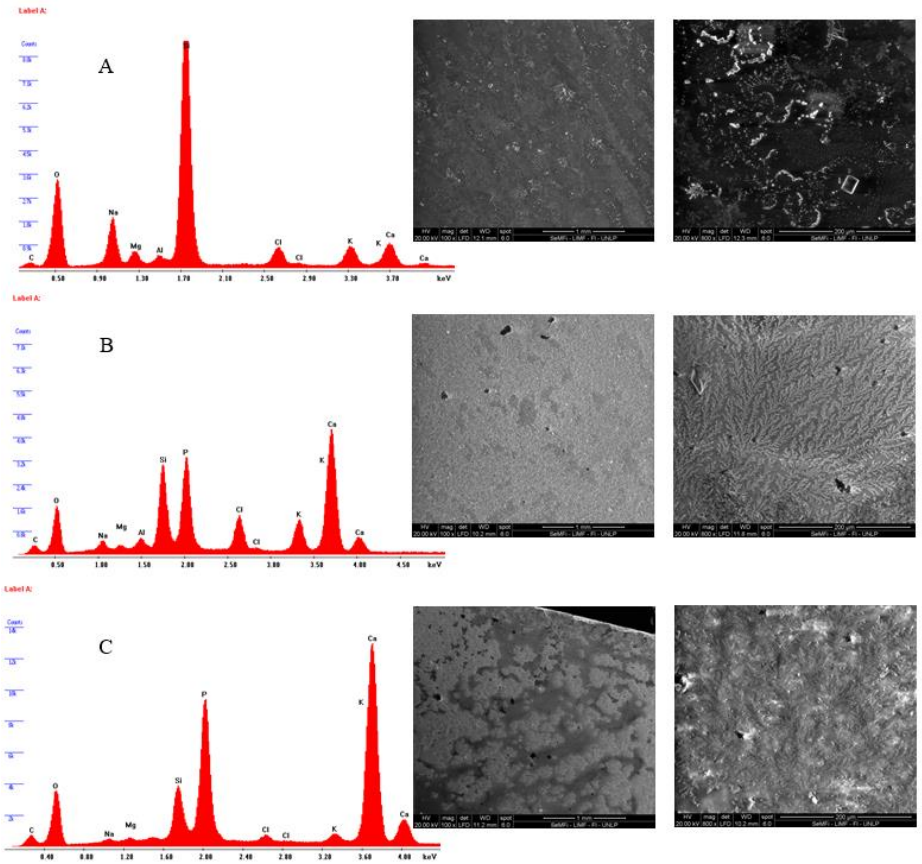

Figure S5. SEM images and EDS profiles of particle-covered glass slides after washing with PBS (twice): (A) Glass slide without particles (control); (B) Ap; (C) ApCOO⁻ (10%).

8. Biological standard procedures

8.1 Cell cultures

Mouse embryo fibroblasts Balb/C 3T3 cells were grown as monolayer in T-25 flasks with D-MEM culture medium supplemented with 10% inactivated fetal calf serum, 50 IU/mL penicillin and 50 mg/mL streptomycin sulfate (complete culture medium, CCM) at 37 ºC in a 5% CO_2 humid atmosphere. Cells were counted in an improved Neubauer hemocytometer and viability was determined by the Trypan blue exclusion method. In all cases, viability was higher than 98%.

8.2 Cell viability assays

AO staining. For this purpose, 24×24 mm glass slides were immersed in 23.0 g L^{-1} of nanoparticles alcoholic suspensions (Ap and $ApCOO^-$ (10%)), the solvent evaporated, and the whole system sterilized. The particle-covered glass slides were introduced in a 10 cm Petri dish which was then seeded with 5×10^5 cell suspension. After 24 h of incubation at 37 ºC in complete culture medium and 5% CO_2 humid atmosphere, the medium was discarded and the slides washed twice with PBS and stained with AO dye prior fluorescence microscopy observation. Balb/C 3T3 cells cultured on glass slides without treatments were used as negative controls.

Scanning Electron Microscopy (SEM) images (and the corresponding EDS profiles) of particle-covered glass slides before and after washing (twice) with PBS demonstrated that particles remain covering the surface after the washing procedures, as shown in Figures S4 and S5.

MTT assay. It was performed using metabolic competence by the colorimetric method of Mosmann [Mosmann, T. *J. Immunol. Methods* **1983**, *65*, 55-63. https://doi.org/10.1016/0022-1759(83)90303-4] as modified by Twentyman and Luscombe [Twentyman, P.R.; Luscombe, M. *Br. J. Cancer* **1987**, *56*, 279-285. https://doi.org/10.1038/bjc.1987.190]. Briefly, 50 µL volume of 11.5 g L^{-1} alcoholic suspension of either Ap or $ApCOO^-$ (10%) were placed in individual wells of a 96-multiwell plate and the solvent evaporated. To 48 of these wells, ca. 2.7×10^4 cells per well were added and cultured at 37 ºC in 5% CO_2 humid atmosphere in CCM. The remaining wells were used as controls to which only CCM was added. After 24 h of incubation, the culture medium was discarded and each well washed twice with PBS and fresh medium containing MTT reagent to a final concentration of 1 mg/mL was added. After 3 h incubation, the MTT solution was discarded and cells washed with PBS. Color was developed by the addition of 100 µL DMSO to each well for cell lysis and dissolution of formazan crystals. The plate was shaken for 10 min and the absorbance was measured at 560 nm using an automatic ELISA plate reader (BioTekµQuant). Absorbance change corrected for the absorbance measured in the absence of cells (controls) is assumed to be directly proportional to the number of viable cells. The MTT reduction activity was expressed as a percentage of the control cells, (A-B)/A×100, with A and B the absorbance of control and treated cells, respectively. Each assay was repeated three times in independent experiments.

Data were analyzed using one-way ANOVA test and multiple comparisons were made using *p* values corrected by the Bonferroni method.